The International Journal of Advanced Manufacturing Technology (2020) 108:809–820
https://doi.org/10.1007/s00170-020-05408-5

ORIGINAL ARTICLE

Performances of Ni_3Al-based intermetallic IC10 in creep-feed grinding

Xiaoxiang Zhu [1,2] · Wenhu Wang [1,2] · Ruisong Jiang [3] · Xiaofen Liu [1,2] · Kunyang Lin [1,2]

Received: 29 July 2019 / Accepted: 5 May 2020 / Published online: 22 May 2020

Abstract

Ni_3Al-based intermetallic IC10 exhibits prominent high-temperature performance (e.g., high melting points, resistant to gas corrosion, and creep resistance); it acts as an ideal material employed to manufacture aero-engine turbine blades. Since the internal structure of the Ni_3Al-based intermetallics differs from that of the conventional superalloy, its grindability significantly limits its application. Grinding parameters are vital factors affecting the surface quality of Ni_3Al intermetallic IC10. In the present study, single-factor and orthogonal experiments were performed to ascertain the grinding temperature, grinding force, and grinding surface quality of Ni_3Al-based intermetallic IC10. As revealed from the conclusion drawn in this study, surface quality and grinding force were considerably affected by cutting depth and feed rate, whereas they were less affected by wheel speed. The process of grinding with high feed rate or deep cutting depth would lead to the production of grooves, debris, delamination, and other defects on the test sample surface. The grinding temperature was deeply affected by the cutting depth. The empirical formulas of the relationships between process parameters and grinding temperature and force were calculated by orthogonal experiments, thereby verifying the correctness of single-factor experiments. Small cutting depth and low feed rate can improve surface integrity and reduce grinding surface defects.

Keywords IC10 · Grinding temperature · Grinding · Grinding force · Surface quality

1 Introduction

As fueled by the advancement of the aviation industry, aero-engine has been increasingly demanded. As an essential component of aero-engine, turbine blades are critical to the function of the whole aircraft. Ni_3Al-based superalloys IC10 refers to a novel generation of aero-engine turbine blade material. Unlike other nickel-based superalloys, the Ni_3Al-based superalloys IC10 pertains to an intermetallic, namely, a compound where a metal and another metal, a metal and a metalloid, are bonded by a metal bond or a covalent bond. Ni_3Al-based intermetallics exhibit considerable prominent properties (e.g., high strength and melting point, high temperature fatigue-resistant, as well as a positive temperature effect of yield strength below the peak temperature) [1–3]. For the mentioned excellent properties, Ni_3Al-based intermetallics have been extensively employed in civil and military industries. Superalloys are typical difficult-to-machine materials for its high hardness, high strength, and low thermal diffusivity [4]. Hardening layer, grain deformation layer, and remelting layer occur commonly on the superalloy surface in the processing course. In recent decades, numerous researchers analyzed the grinding of nickel-based superalloys. Dai et al. [5–7] performed grinding experiments to investigate the grinding temperature, grain wear, and material removal rate of superalloy Inconel 718. In [6], a single diamond grain was adopted to perform the grinding experiments; and grain wear is classified into different types according to the friction, plowing, and cutting time in the course of grinding. Chen et al. [8] performed grinding experiments on superalloy Inconel 718; they developed a method to prevent grinding burn and elevated the material removal rate. Zhao et al. [9] employed a CBN wheel to perform profile grinding of directionally solidified superalloy

✉ Ruisong Jiang
jiangrs@scu.edu.cn

1 1 Key Laboratory of High Performance Manufacturing for Aero Engine, Ministry of Industry and Information Technology, School of Mechanical Engineering, Northwestern Polytechnical University, Xi'an 710072, Shaanxi, China

2 Engineering Research Center of Advanced Manufacturing Technology for Aero Engine, Ministry of Education, School of Mechanical Engineering, Northwestern Polytechnical University, Xi'an 710072, Shaanxi, China

3 School of Aeronautics and Astronautics, Sichuan University, Chengdu 610065, Sichuan, China

DZ125; they reported that altering the maximum grinding thickness could reduce the specific grinding energy.

Creep-feed grinding (CFG), as an advanced processing method, exhibits a large cutting depth; it is also referred to as creep-feed deep grinding. CFG exhibits high grinding surface quality and high processing efficiency, so it is commonly adopted for difficult-to-machine materials processing. Gu et al. [10] applied microcrystalline alumina grinding wheel and brown alumina grinding wheel for DD6 superalloy CFG. Besides, the analyses were conducted on the grinding force, temperature, surface quality, and wheel wear. As suggested from their results, microcrystalline alumina grinding wheel is preferable to brown alumina grinding wheel in grinding surface quality, grinding force, and temperature. Ding et al. [11] ascertained the grinding performance and surface quality of K424 superalloy during CFG; they also measured the processing parameters applying to straight groove processing. For the large cutting depth of CFG, the grinding temperature could be too high, and the workpiece surface could be burned. Wang et al. [12] built a thermal model based on the grinding force during CFG, which is capable of predicting the workpiece temperature. Moreover, their experimental results demonstrated the correctness of the prediction model. Marco et al. [13] proposed an approach to monitor the grinding surface temperature, which can obtain the maximal grinding temperature and the evolution of the temperature. Several scholars adopted auxiliary means to lower the risk of surface burned during CFG. For instance, Abdullah et al. [14] added longitudinal ultrasonic vibration to grinding wheel during CFG. The grinding force was studied by simulation and experiments. As suggested from the experimental results, vertical and horizontal grinding forces decreased by 27% and 22%, respectively.

In recent years, the investigation on Ni_3Al-based intermetallics placed a general emphasis on its material properties, mechanical properties, and preparing methods [15]. Machinability is considered a vital aspect of Ni_3Al-based intermetallics. The study here focused on the grinding properties of Ni_3Al-based intermetallics.

2 Experiments

The sample material is Ni_3Al-based intermetallic IC10, namely, a solidified columnar crystal with anisotropy. The samples had the width, length, and height of 10, 20, and 10 mm, respectively. Tables 1 and 2 list the constitution and physical properties of IC10, respectively. IC10 pertains to face-centered cubic crystal, and the machined surface of this experiment paralleled to [001] crystal direction.

Table 2 Physical properties of IC10

Contents	Value
Density ρ (g/cm^3)	7.9
Melting point T (°C)	1640
Microhardness (HV)	414
Crystal structure	B2

The Chevalier FSG-B818CNC grinder was employed to perform grinding experiments. The grinding wheel is made of brown corundum and white corundum mixed wheel, exhibiting the particle size of 80. The grinding method used was down-grinding, and the grinding diagram is illustrated in Fig. 1. A water-based coolant was sprayed in the grinding course. After grinding a sample, the grinding wheel should be dressed with a wheel dresser to keep the grinding wheel sharp. Single-factor experiments and orthogonal experiments were designed based on the experiential scale of grinding parameters. Tables 3 and 4 list the experimental parameters of the CGF single-factor experiments and orthogonal experiments, respectively.

3 Grinding performance of IC10

3.1 Grinding force and force ratio

Grinding force is a significant index of the grinding process, which has important influence on grinding surface roughness, grinding temperature, and plastic deformation [16, 17]. The grinding force incorporates the tangential force F_t (N) and the normal force F_n (N), and their relationships with the horizontal force F_h (N) and the vertical force F_v (N) measured by the dynamometer are presented in Fig. 2, meeting the formula below [18].

$$F_t = F_v sin\theta + F_h cos\theta \tag{1}$$

$$F_n = F_v cos\theta - F_h sin\theta \tag{2}$$

Where θ (rad) is the rotating angle, which could be expressed as

$$\theta = \sqrt{a_p/d_s} \tag{3}$$

where d_s (mm) is the wheel diameter and a_p (mm) is the cutting depth.

Table 1 Constitution of IC10 (wt%)

Elements	Co	Ta	Al	Cr	W	Hf	Mo	C	B	Ni
wt%	11.5~12.5	6.5~7.5	5.6~6.2	6.5~7.5	4.8~5.2	1.3~1.7	1.0~2.0	0.07~0.12	0.01~0.02	Bal

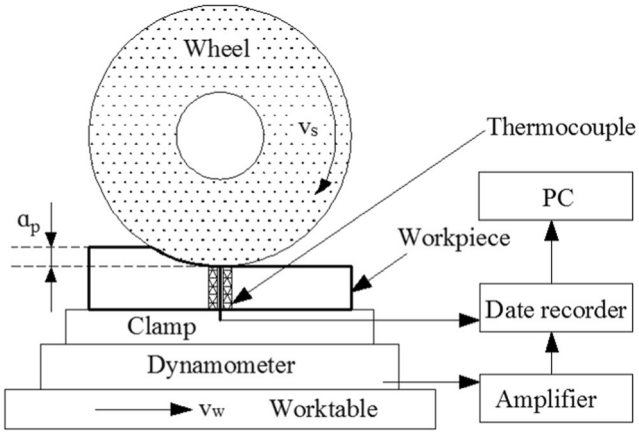

Fig. 1 Diagram of CFG

The impact of grinding parameters on grinding force is illustrated in Fig. 3. As seen in Fig. 3(a), the variation of tangential force F_t with the feed rate is not obvious. At the feed rate less than 150 mm/min, the variation of normal force F_n is not obvious. However, at the feed rate risen from 150 to 250 mm/min, the normal force F_n increases from 651 to 876 N. Accordingly, the feed rate has a smaller effect on the tangential force F_t and a larger effect on the normal force F_n, and at the feed rate over 150 mm/min, the normal force F_n increases rapidly. Figure 3(b) indicates that at the cutting depth increases from 0.1 to 0.9 mm, the tangential force F_t increases from 230 N to 432 N, and the normal force F_n increases from 313 to 896 N. As seen in Fig. 3(c), as the wheel speed increases, the tangential force F_t decreases from 455 to 284 N, but the normal force F_n decreases only from 648 to 619 N. The variation of grinding force with the three grinding parameters is associated with the variance of maximum undeformed chip thickness (UCT). The relationships between UCT $h_{\max}$ (mm) and grinding parameters are expressed in Eq. (4) [19].

$$h_{max} = \left(\frac{4v}{v_s N_d C}\sqrt{\frac{a_p}{d_s}}\right)^{1/2} \tag{4}$$

where a_p (mm) is the cutting depth, v_s (m/s) is the grinding wheel speed, v_w (mm/min) is the feed rate, N_d is effective grain number per unit area, d_s (mm) refers to the diameter of the wheel, and C refers to a constant in connection with the angle of the abrasive particle tip. The grinding force varies with the feed rate for two reasons. On the one hand, the UCT of a single abrasive grain increases as the increase of workpiece feed rate, and the grinding force of the effective abrasive grain increases. On the other hand, setting the cutting depth constant, as the workpiece feed rate increases, the material removal rate of the workpiece increases, and the cutting thickness of the single abrasive grain increases, inevitably resulting in an increase in the grinding force. The grinding force varies with the cutting depth also for two reasons. On the one hand, as the cutting depth increases, the UCT of the single abrasive grain increases, and the grinding force of the single abrasive grain increases. On the other hand, the rise in cutting depth makes the grinding arc length of grinding wheel larger, and the number of dynamic effective abrasive grain involved in grinding in the grinding arc area increases, leading to the rise in the total grinding force. According to Eq. (4), decreasing grinding wheel speed would result in the rise in UCT. The rise in UCT led to greater friction between abrasive particle and grinding surface, so the grinding force increases.

Table 3 Single-factor experiments of CFG

No.	Grinding parameters	Level				
		−2	−1	0	1	2
1	Feed rate v_w (mm/min)	50	100	150	200	250
2	Cutting depth a_p (mm)	0.1	0.3	0.5	0.7	0.9
3	Wheel speed v_s (m/s)	12	17	22	27	32

Given the results of orthogonal experiments, the least square method can be adopted to fit the relational expression between grinding force and grinding parameters. The relation is expressed as follows:

$$F_t = 117.9 v_w^{0.21} a_p^{0.27} v_s^{-0.27} \tag{5}$$

$$F_n = 197.8 v_w^{0.29} a_p^{0.32} v_s^{-0.04} \tag{6}$$

Equations (5) and (6) show that the indices of a_p and v_w are positive, that is, the cutting depth and the workpiece feed rate are positively correlated with the grinding force. The index of v_s is negative, that is, the grinding wheel speed is negatively correlated with the grinding force. Cutting depth has the most significant impact on grinding force, and the second is workpiece feed rate. The regression correlation coefficient of tangential grinding force is 0.74, and the correlation coefficient of normal grinding force is 0.75. It is therefore suggested that the correlation is credible.

Grinding force ratio F_n/F_t refers to an essential parameter in grinding. The magnitude of the grinding force ratio can reflect the wear of the grinding wheel in the grinding course. A large grinding force ratio indicates a more severe wheel wear in the grinding course. $Q_{w'}$ is the material removal rate in unit grinding width, and its calculation formula is:

$$Q_{w'} = a_p v_w. \tag{7}$$

Figure 4 gives the curve of force ratio F_n/F_t versus the material removal rate Q_w. When $Q_{w'}$ increases from 0.25 to 2.25 $mm^3/(mm\ s)$, the grinding force ratio F_n/F_t increases from 1.36 to 2.07. Equation (7) shows that when the feed rate v_w is constant, $Q_{w'}$ is positively related with the cutting depth a_p. Accordingly, as the cutting depth increases, the sharpness

Table 4 Orthogonal experiments of CFG

No.	Grinding parameters			Grinding force		Grinding temperature T (°C)
	Feed rate v_w (mm/min)	Cutting depth a_p (mm)	Wheel speed v_s (m/s)	F_t (N)	F_n (N)	
1	50	0.1	12	168	277	293
2	50	0.3	17	219	299	586
3	50	0.5	22	249	395	917
4	50	0.7	27	296	444	983
5	100	0.1	17	270	372	343
6	100	0.3	12	344	397	566
7	100	0.5	27	397	567	892
8	100	0.7	22	403	618	1036
9	150	0.1	22	231	329	341
10	150	0.3	27	256	370	754
11	150	0.5	12	374	490	867
12	150	0.7	17	395	527	966
13	200	0.1	27	261	379	656
14	200	0.3	22	289	492	845
15	200	0.5	17	395	630	1082
16	200	0.7	12	422	787	1113

of the grinding wheel decreases and the wear becomes more serious.

3.2 Grinding temperature

The surface quality of the test sample is significantly affected by the grinding temperature [20]. A temperature too high will cause subsurface remelting and surface burns. To ascertain the grinding temperature, artificial semi-thermocouples were manufactured with IC10 samples and constantan wires. Given the Seebeck effect, the thermodynamic potential of IC10 and constantan wires at different temperatures was ascertained. The relationships between thermoelectric potential and temperature were fitted according to the measurement results, and the calibration straight line of temperature was obtained (Fig. 5).

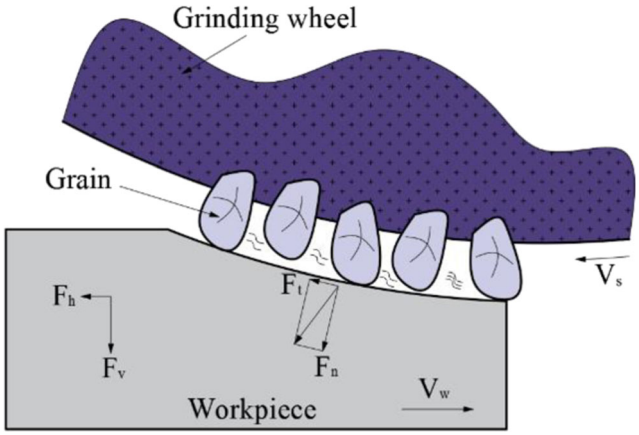

Fig. 2 Diagram of grinding force and measured force

According to the fitting result, the relational expression between the thermoelectric potential and the temperature is:

$$T = 54.43 + 11.53U \tag{8}$$

Figure 6 indicates the impact of grinding parameters on grinding temperature in single-factor experiment. Figures 6(a, b) clearly show that the grinding temperature displayed noticeable positive correlations with feed rate and cutting depth. As the feed rate ranges from 50 to 250 mm/min, the measured temperature ranges from 908 to 1104 °C. As the cutting depth ranges from 0.1 to 0.5 mm, grinding temperature ranges from 320 to 999 °C, and as the cutting depth ranges from 0.5 to 0.9 mm, the grinding temperature increased from 999 to 1092 °C. Thus, when the cutting depth value is below 0.5 mm, the grinding temperature is sensitive to the augment of cutting depth. A change in cutting depth within this range will cause a sharp increase in temperature. At the cutting depth value above 0.5 mm, grinding temperature is insensitive to cutting depth. The reason that grinding temperature increases with the variation of cutting depth or workpiece feed rate is that the rise in cutting depth or workpiece feed rate will result in an increase in grinding force, and the plow force and friction between the wheel and grinding surface will increase, and the course of working needs to consume more energy. Moreover, the rapid rise of grinding temperature is also related to the boiling effect of coolant [21–23]. During CFG, the cutting depth has an important effect on the grinding process, the coolant is easy to boil, and the cooling effect is very limited after the coolant boiling.

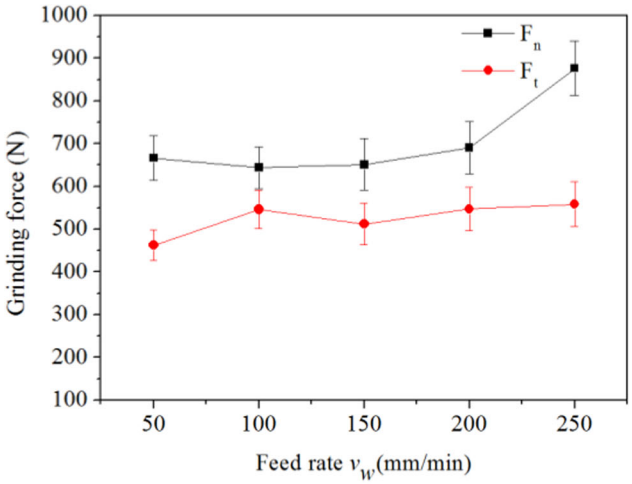

(a) a_p=0.5 mm, v_s=22 m/s

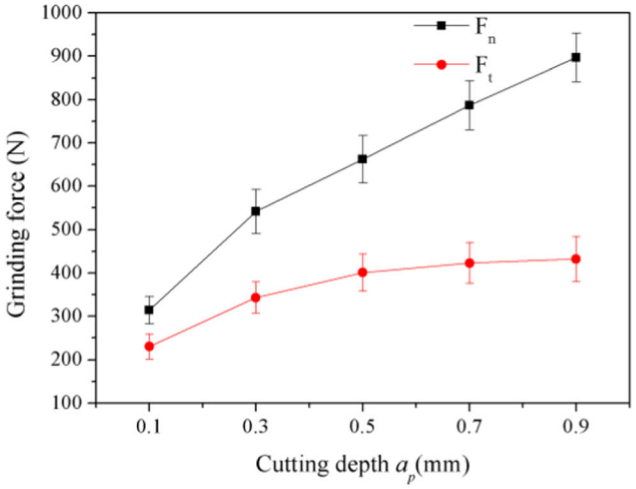

(b) v_w=150 mm/min, v_s=22 m/s

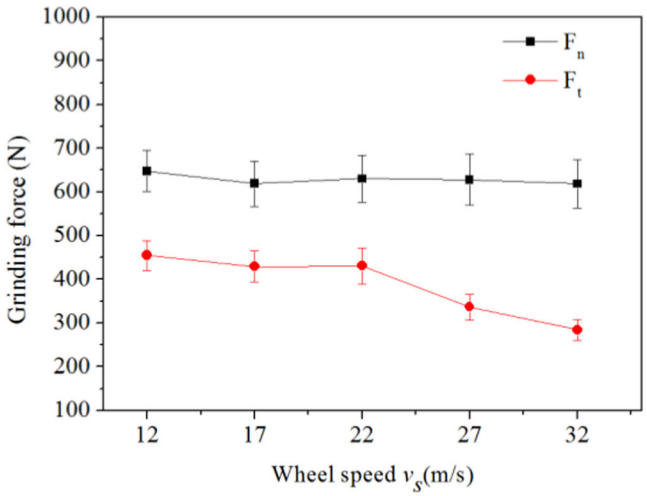

(c) a_p=0.5 mm, v_w=150 mm/min

Fig. 3 Impact of grinding parameters on grinding force

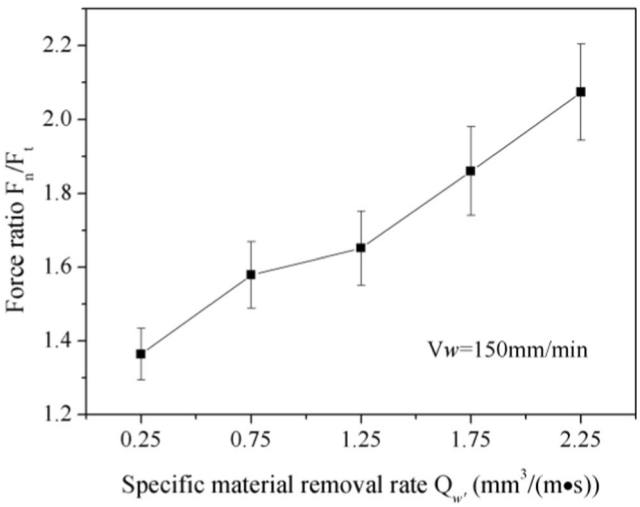

Fig. 4 Variation of force ratio versus specific material removal rate

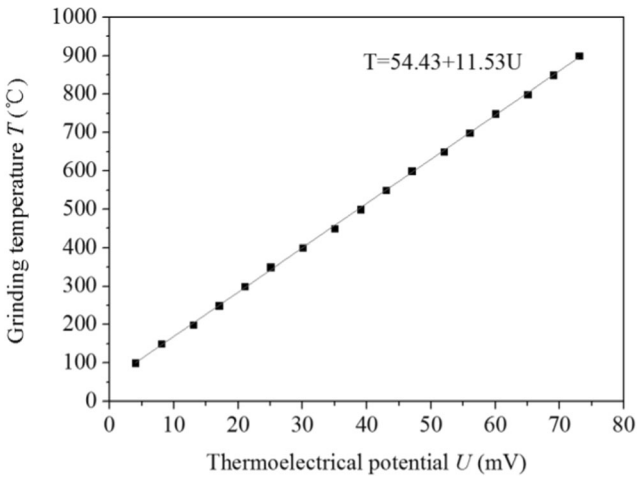

Fig. 5 Calibration straight line of grinding temperature

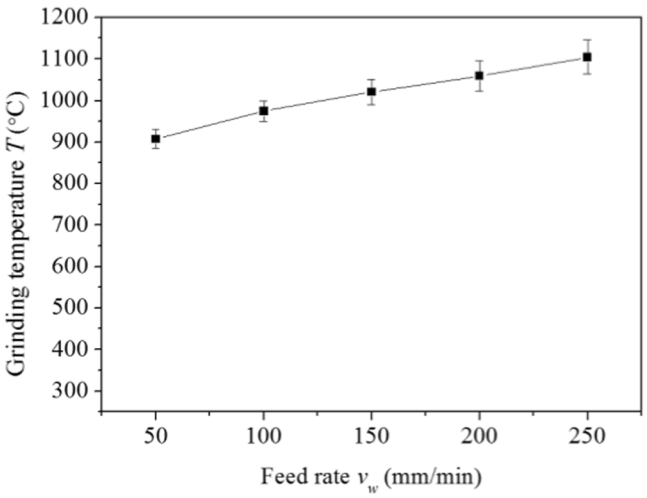

(a) a_p=0.5 mm, v_s=22 m/s

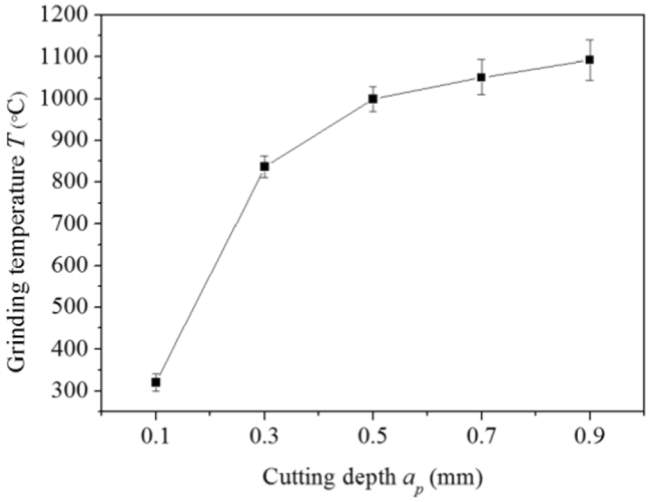

(b) v_w=150 mm/min, v_s=22 m/s

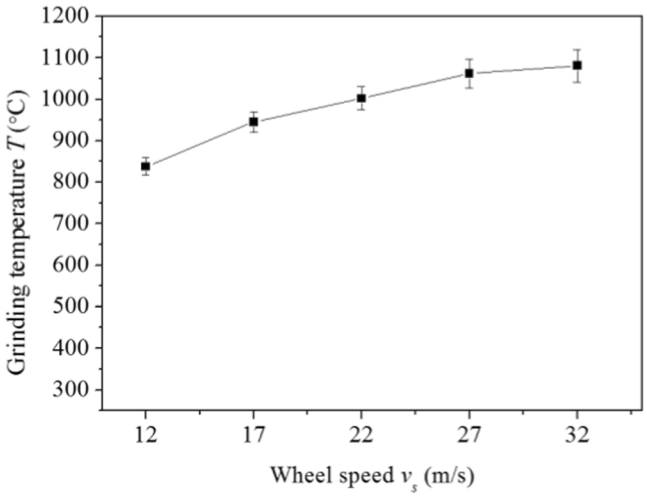

(c) a_p=0.5 mm, v_w=150 mm/min

Fig. 6 Effect of grinding parameters on grinding temperature

As illustrated in Fig. 6(c), grinding temperature increases with the rise in grinding wheel speed. The grinding temperature increases from 838 to 1081 °C as the wheel speed increased from 12 to 32 m/s. The rise of grinding wheel speed will increase the abrasive grains in contact with the workpiece in unit time, and more grinding heat will be produced in unit time, thereby leading to the rise in the grinding temperature.

Given the results of the orthogonal experiment, the relational expression parameters between grinding temperature and grinding parameters can be estimated by the least square method as:

$$T = 240.0 {v_w}^{0.21} {a_p}^{0.48} {v_s}^{-0.23} \quad (9)$$

According to the estimation by Eq. (8), grinding temperature is positively correlated with the cutting depth, feed rate, and grinding wheel speed. The grinding temperature is most affected by the cutting depth, with wheel speed ranked behind. This complied with the results of the single-factor experiment, thereby demonstrating the correctness of the single-factor experiment.

4 Surface integrity of IC10

4.1 The roughness and surface topography

Generally speaking, grinding is the final process of machining, so the surface roughness and morphology after grinding is critical. Figures 7 (a), (b), and (c) indicate the effect of workpiece feed rate v_w, cutting depth a_p, and grinding wheel speed

v_s on grinding surface roughness, respectively. According to Fig. 7(a), when feed rate v_w increases from 50 to 150 mm/min, the grinding surface roughness of test sample ranges from 0.085 to 0.148 μm, whereas at the feed rate rising from 150 to 250 mm/min, the surface roughness increases from 0.148 to 0.571 μm. Accordingly, at the feed rate less than 150 mm/min, the variation of surface roughness is relatively stable. Once the feed rate is greater than 150 mm/min, the surface roughness will increase rapidly. According to Fig. 7(b), as the cutting depth a_p ranges from 0.1 to 0.5 mm, the surface roughness of test sample ranges from 0.122 to 0.152 μm, while the surface roughness ranges from 0.152 to 0.567 μm as the cutting depth increases from 0.5 to 0.9 mm. Thus, in the cutting depth range between 0.1 and 0.5 mm, the rise in cutting depth has less effect on the surface roughness. When the cutting depth varies from 0.5 to 0.9 mm, the rise in cutting depth has a great impact on the surface roughness. The UCT has a remarkable effect on grinding surface roughness [24]. According to Eq. (4), with the augment of feed rate v_w and cutting depth a_p, the UCT augment and hence the grinding force increases. Large grinding forces cause drastic plastic deformation of the grinding surface, which usually led to increased surface roughness.

Figure 7(c) suggests that as the grinding wheel speed v_s ranges from 12 to 22 m/s, the surface roughness of test sample reduced from 0.325 to 0.154 μm. However, when the grinding wheel speed v_s ranges from 22 to 32 m/s, the surface roughness augment from 0.154 to 0.171 μm. Theoretically, increasing the wheel speed v_s will reduce the surface roughness and grinding force. However, the surface roughness increases when the wheel

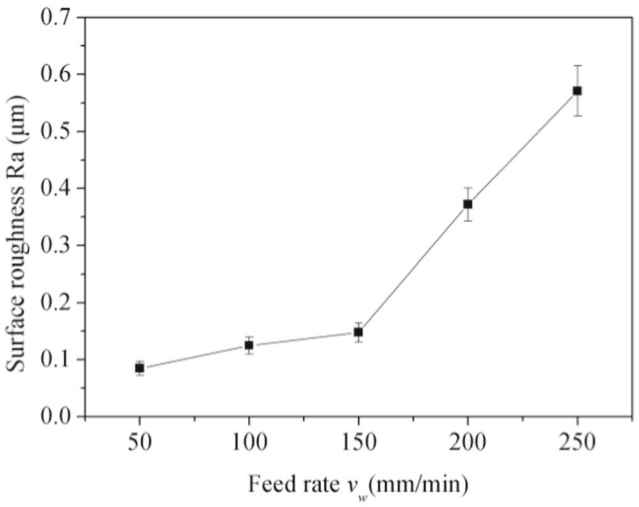

(a) a_p=0.5 mm, v_s=22 m/s

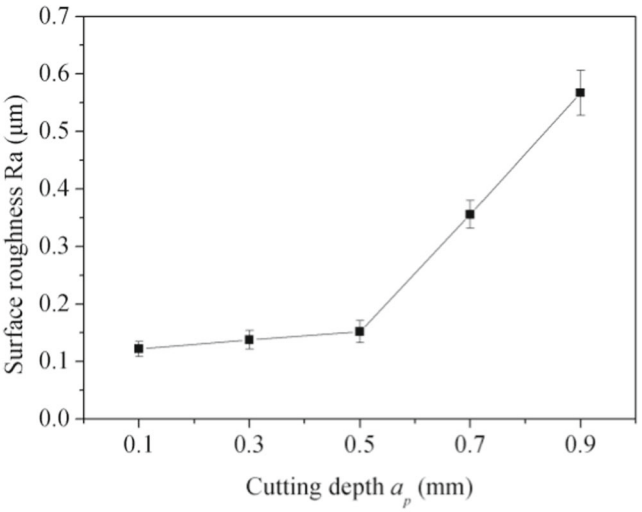

(b) v_w=150 mm/min, v_s=22 m/s

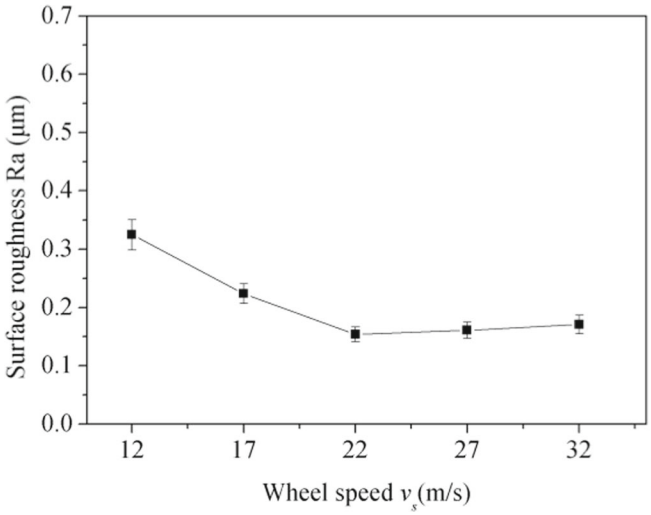

(c) a_p=0.5 mm, v_w=150 mm/min

Fig. 7 Effect of grinding parameters on surface roughness

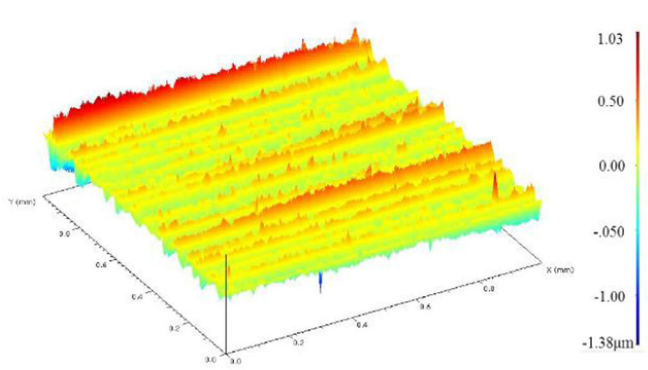

(a) v_s=22 m/s, a_p=0.5 mm, v_w=50 mm/min

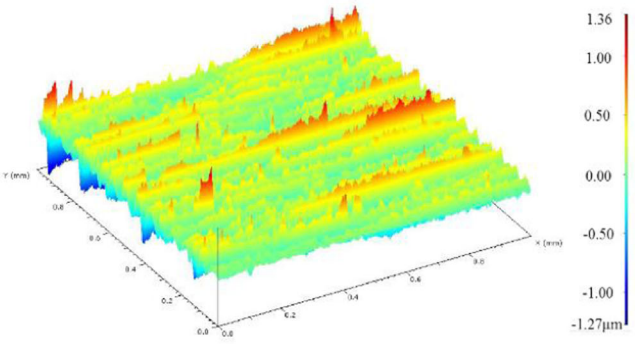

(b) v_s=22 m/s, a_p=0.5 mm, v_w=100 mm/min

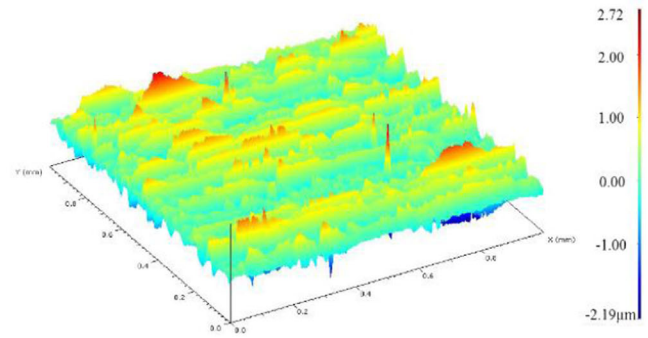

(c) v_s=22 m/s, a_p=0.5 mm, v_w=150 mm/min

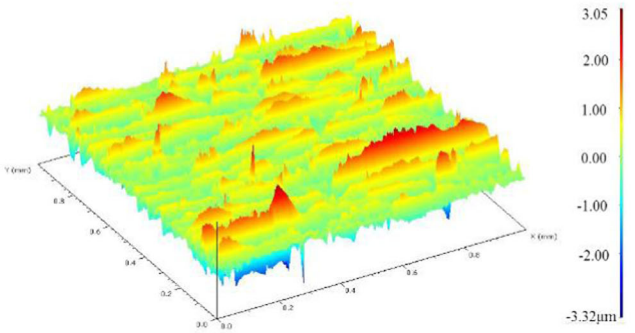

(d) v_s=22 m/s, a_p=0.5 mm, v_w=200 mm/min

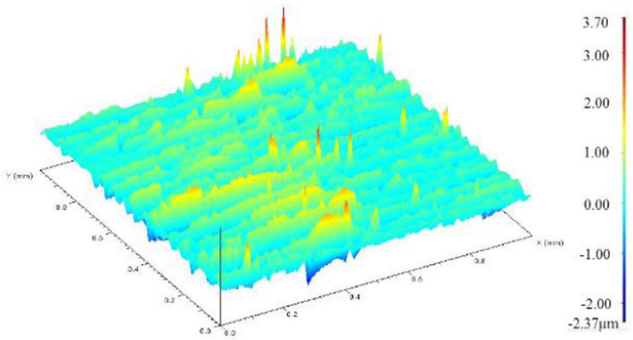

(e) v_s=22 m/s, a_p=0.5 mm, v_w=250 mm/min

Fig. 8 Influence of feed rate on the 3D topography of grinding surface

speed is overly high. The reason is that when the wheel speed is large, the heat generated in the grinding arc area increases. Under the high temperature of grinding, the grinding wheel adheres to the workpiece, and the cutting ability of the grinding wheel decreases, which makes the grinding surface quality deteriorate rapidly and the surface roughness increase [25].

Since the grinding surface roughness is most heavily affected by feed rate v_w among the three grinding parameters, Mahr XT 20 3D surface profile scanner was employed to scan the grinding surface topography at different feed rates. Figure 8 suggests that under the other identical parameters, the grinding surface has a lower hollow and a higher protrusion as the feed rate increases. The effect of feed rate on 3D topography of grinding surface complied with the effect on the surface roughness.

4.2 Surface and subsurface defects

From the mentioned analysis, the surface topography and surface roughness are significantly affected by cutting depth and

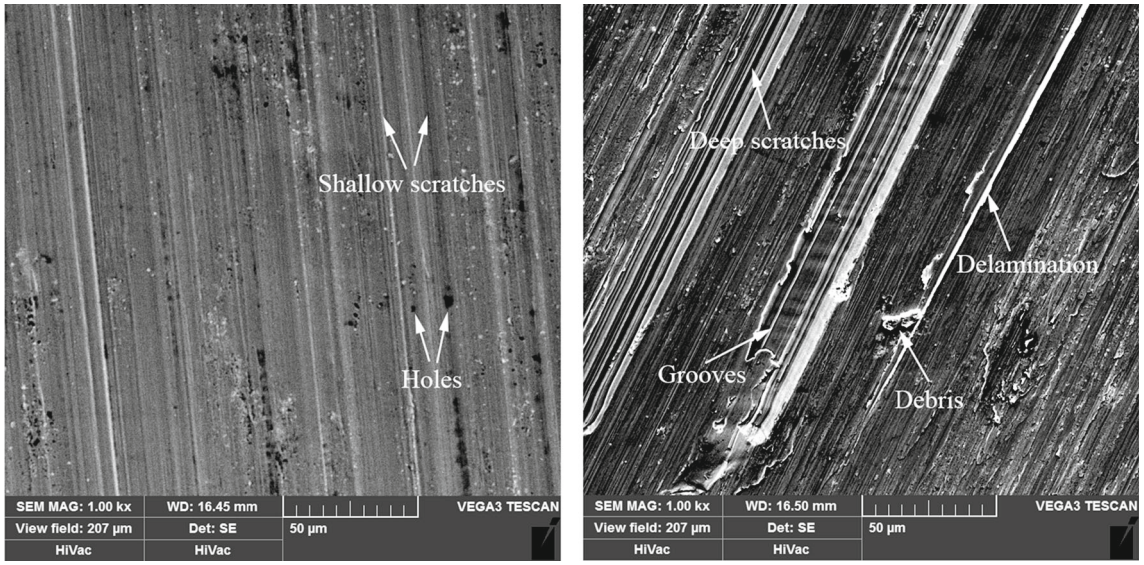

(a) a_p=0.5 mm, v_s=22 m/s, v_w=50 mm/min (b) a_p=0.5 mm, v_s=22 m/s, v_w=250 mm/min

Fig. 9 Grinding surface SEM topography with different feed rates

feed rate. The surfaces exhibiting different grinding parameters were observed under a scanning electron microscope (SEM).

Figure 9 gives the SEM topography of the test sample grinding surface at different feed rates. According to Fig. 9, the test sample grinding surface is relatively smooth at a feed rate of 50 mm/min, the major defects of the grinding surface are holes and shallow scratches; at the feed rate of 250 mm/min, the main defects on the grinding surface are deep scratches, grooves, debris, and delamination.

Figure 10 presents the SEM topography of the grinding surface with different cutting depths. At the cutting depth of 0.1 mm, the topography of the test sample grinding surface is similar to that at the feed rate of 50 mm/min. The major defects of the grinding surface are shallow scratches and holes. At the cutting depth of 0.9 mm, the main defects of the test sample grinding surface are cracks, delamination, and large unremoved areas, and the surface appeared to be highly rough.

As the cutting depth and feed rate increase, the UCT increases, which results in the increase of grinding force. On the one hand, large grinding forces cause greater plastic deformation of the grinding surface. On the other hand, large grinding force increases the force on the abrasive grain of the grinding wheel, making it easier to fall off from the grinding wheel.

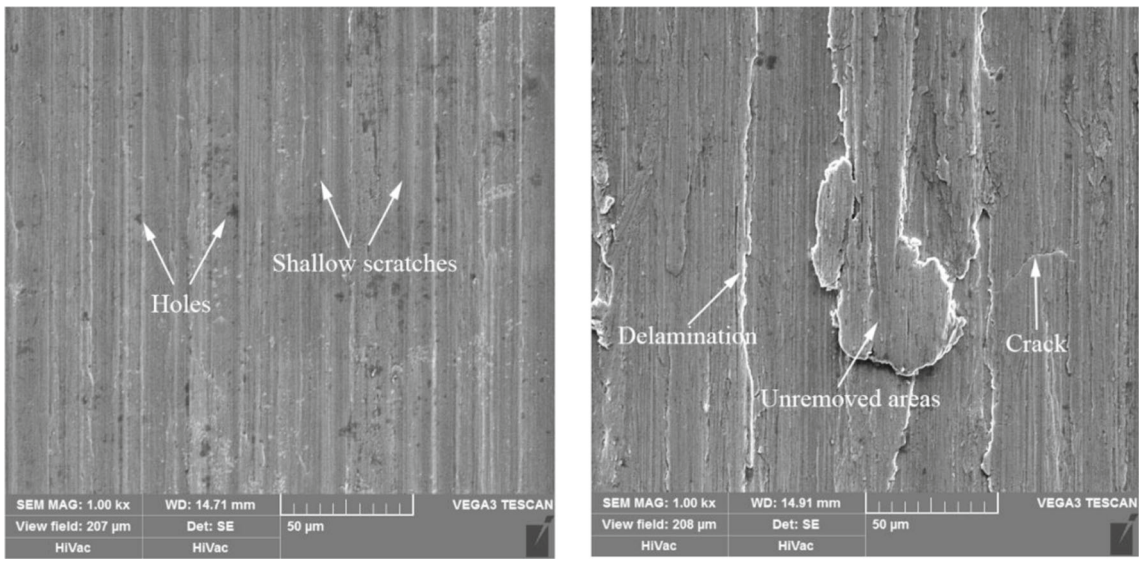

(a) a_p=0.1 mm, v_s=22 m/s, v_w=150 mm/min (b) a_p=0.9 mm, v_s=22 m/s, v_w=150 mm/min

Fig. 10 Grinding surface SEM topography with different cutting depths

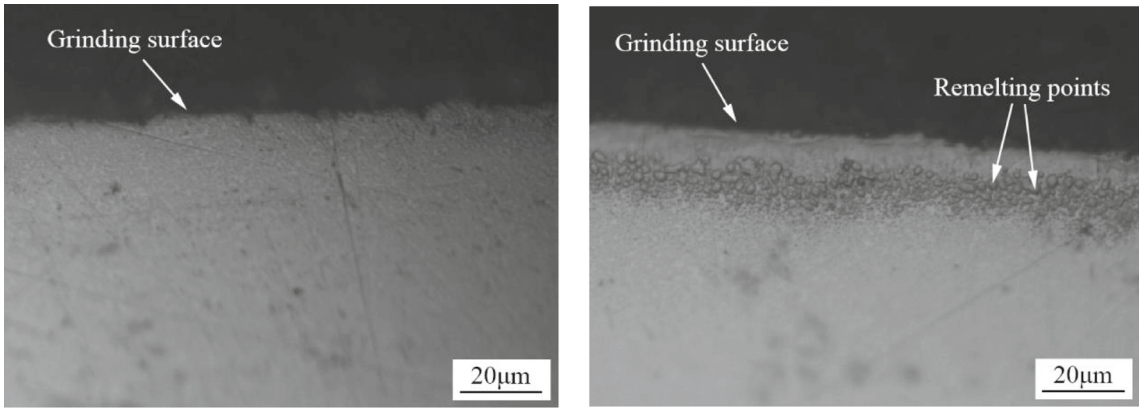

(a) a_p=0.5 mm, v_s=22 m/s, v_w=50 mm/min (b) a_p=0.5 mm, v_s=22 m/s, v_w=250 mm/min

Fig. 11 The microstructure below the grinding surface with different feed rates

Under the extrusion effect of the grinding wheel, the dropped abrasive grains carve and plow on the surface of the workpiece, resulting in irregular scratches on the workpiece surface.

Figures 11 and 12 illustrate the microstructure of the grinding surface at different feed rates and cutting depths. According to Fig. 11(a), at the minimum feed rate of 50 mm/min, the microstructure of the subsurface layer is similar to that inside the sample, and slight microstructure change is identified. Figure 11(b) shows that at the maximum feed rate of 250 mm/min, there are considerable remelting points between 10 and 20 μm below the grinding surface. The width of the remelting region formed by the remelting points is about 10 μm. The grinding temperature is 908 °C at the minimum feed rate of 50 mm/min, while the grinding temperature is 1104 °C at the maximum feed rate of 250 mm/min. The high grinding temperature results in considerable remelting points in the subsurface layer of the grinding surface.

As seen from Fig. 12(a), there is no obvious microstructure defect in surface and subsurface at the cutting depth of 0.1 mm. As seen from Fig. 12(b), at the cutting depth of 0.9 mm, remelting areas appear in surface layer and remelting points appear in subsurface layer. The corresponding grinding temperature is 320 °C at the cutting depth of 0.1 mm, and the corresponding grinding temperature is 1092 °C at the cutting depth of 0.9 mm.

Thus, large cutting depth and feed rate would rise grinding temperatures, probably causing remelting defects in the surface and subsurface. Large cutting depth and feed rate should be avoided in the grinding process.

4.3 The microhardness

The microhardness of the ground surface changes under the dual function of grinding heat and grinding force. The Vickers hardness of the IC10 superalloy matrix material is 414 HV. The previous analysis revealed that the workpiece feed rate and cutting depth exerted a prominent effect on the grinding force and the grinding temperature.

The effects of different cutting depths and feed rates on the microhardness of the test sample grinding surface are analyzed below. Figure 13(a) indicates that the microhardness at 10 μm below the grinding surface is 453 HV at the minimum

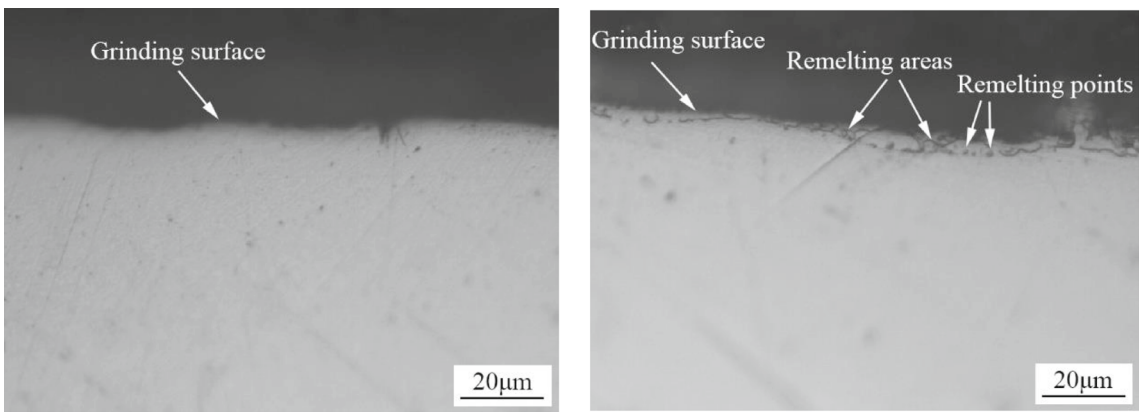

(a) a_p=0.1 mm, v_s=22 m/s, v_w=150 mm/min (b) a_p=0.9 mm, v_s=22 m/s, v_w=150 mm/min

Fig. 12 The microstructure below the grinding surface with different cutting depths

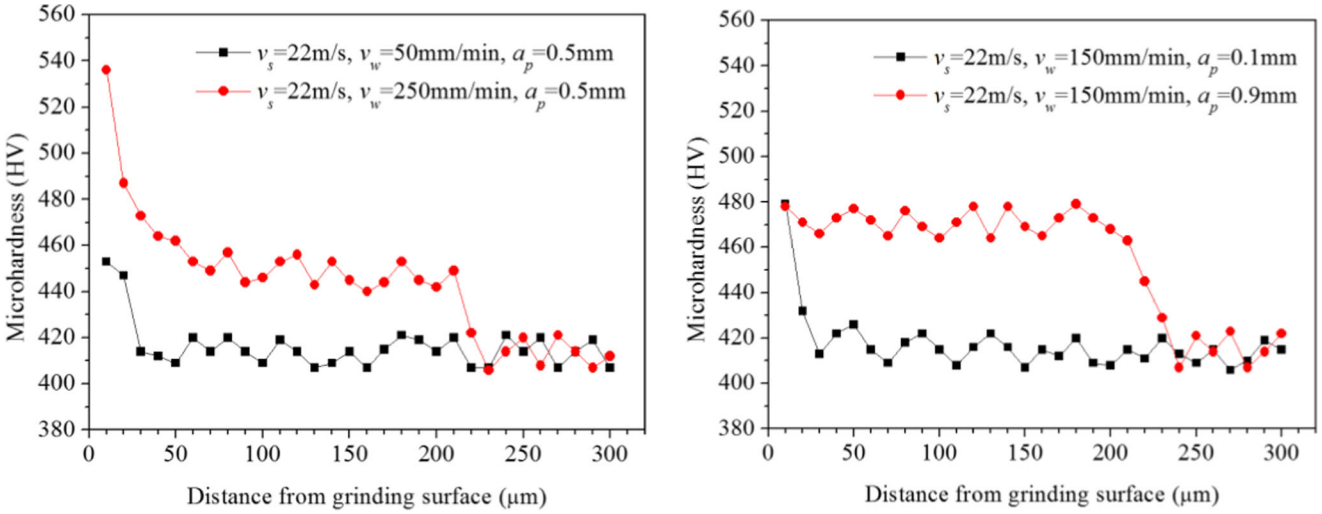

(a) different feed rates (b) different cutting depths

Fig. 13 The effects of different grinding parameters on the microhardness of the grinding subsurface

feed rate of 50 mm/min, 9.4% higher than the microhardness of the matrix material, and the thickness of the microhardness changing layer is approximately 30 μm. At the maximum feed rate of 250 mm/min, the microhardness at 10 μm below the grinding surface is 536 HV, 29.5% higher than the microhardness of the matrix material, and the thickness of the microhardness changing layer is about 220 μm.

As shown in Fig. 13(b), the microhardness at 10 μm below the grinding surface is 479 HV at the cutting depth of 0.1 mm, 15.7% higher than the microhardness of the matrix material, and the thickness of the microhardness changing layer is approximately 20 μm. At the cutting depth of 0.9 mm, the microhardness at 10 μm below the grinding surface is 478 HV, 15.5% higher than the microhardness of the matrix material, and the thickness of the microhardness changing layer is approximately 230 μm.

The above analysis indicates that CFG will result in work hardening on the surface of IC10. As the distance from the grinding surface increases, the microhardness decreases and finally approaches the microhardness of the bulk material. Work hardening is primarily caused by grinding force, the greater the cutting depth and feed rate, the greater the grinding force will be. The larger grinding force will lead to a strong plastic deformation on the test sample grinding surface, thereby making the metal lattice seriously distorted and the grain broken, thus preventing the metal from further deformation and increasing the hardness of the grinding surface.

5 Conclusions

The effects of grinding parameters on grinding force, grinding temperature, and surface integrity were investigated during CFG of IC10 superalloy. Single-factor and orthogonal grinding experiments were performed under different feed rates, cutting depths, and grinding wheel speeds. The conclusions drawn include:

(1) During CFG, grinding force displayed obvious positive relationships to workpiece feed rate and cutting depth and obvious negative associations with grinding wheel speed. Cutting depth has the most visible impact on grinding force, with workpiece feed rate ranked behind. The surface roughness displayed noticeable positive correlations with cutting depth and workpiece feed. The surface roughness was negatively related to the grinding wheel speed as the grinding wheel speed was lower than 22 m/s. The surface roughness was positively related to the grinding wheel speed at the grinding wheel speed higher than 22 m/s.

(2) Increasing feed rate, cutting depth and wheel speed would rise the grinding temperature. The cutting depth most obviously impacted grinding temperature, with grinding wheel speed ranked behind.

(3) The larger the cutting depth and feed rate, the more the surface defects would be. The main surface defects included deep scratches, grooves, debris, delamination, and unremoved areas. When cutting depth and workpiece feed rate were overly large, there would be remelting points in the subsurface.

(4) CFG will alter the microhardness of the grinding subsurface. With the rise in cutting depth and workpiece feed rate, the subsurface microhardness value and the thickness of the microhardness changing layer will be elevated. By setting other parameters unchanged, at the feed rate of 50 mm/min and 250 mm/min, the corresponding thickness of the microhardness changing layer under the

grinding surface is 30 μm and 230 μm, respectively. Likewise, with other parameters unchanged, when the cutting depth is 0.1 mm and 0.9 mm, the corresponding thickness of the microhardness changing layer under the grinding surface is 30 μm and 230 μm, respectively.

Funding information This study was supported by NSAF (Grant No. U1830122) and the National Natural Science Foundation of China (Grant No. 51775443).

References

1. Karin G, Luo H, Feng D, LI CH (2007) Ni_3Al-based intermetallic alloys as a new type of high-temperature and wear-resistant materials. J Iron Steel Res Int 14(5):21–25
2. Yamaguchi M, Inui H, Ito K (2000) High-temperature structural intermetallics. Acta Mater 48(1):307–322
3. Zhu SY, Bi QL, Yang J, Qiao ZH, Ma JQ, Li F, Yin B, Liu WM (2014) Tribological behavior of Ni_3Al alloy at dry friction and under sea water environment. Tribol Int 75:24–30
4. Choudhury IA, El-Baradie MA (1998) Machinability of nickel-base super alloys: a general review. J Mater Process Technol 77(1):278–284
5. Dai CW, Ding WF, Xu JH, Chen D, Huang GQ (2017) Investigation on size effect of grain wear behavior during grinding nickel-based superalloy Inconel 718. Int J Adv Manuf Technol 91(5–8):2907–2917
6. Dai CW, Ding WF, Xu JH, Fu YC, Yu TY (2017) Influence of grain wear on material removal behavior during grinding nickel-based superalloy with a single diamond grain. Int J Mach Tools Manuf 113:49–58
7. Dai CW, Ding WF, Xu JH, Xu XP, Fu DK (2017) Effects of undeformed chip thickness on grinding temperature and burn-out in high-efficiency deep grinding of Inconel718 superalloys. Int J Adv Manuf Technol 89(5–8):1841–1852
8. Chen ZZ, Xu JH, Ding WF, Ma CY, Fu YC (2015) Grinding temperature during high-efficiency grinding Inconel 718 using porous CBN wheel with multilayer defined grain distribution. Int J Adv Manuf Technol 77(1–4):165–172
9. Zhao ZC, Fu YC, Xu JH, Zhang ZW, Liu ZW, He J (2016) An investigation on high-efficiency profile grinding of directional solidified nickel-based superalloys DZ125 with electroplated CBN wheel. Int J Adv Manuf Technol 83(1–4):1–11
10. Gu YL, Li HN, Du BC, Ding WF (2019) Towards the understanding of creep-feed deep grinding of DD6 nickel-based single-crystal superalloy. Int J Adv Manuf Technol 100(1–4):445–455
11. Ding WF, Xu JH, Chen ZZ, Su HH, Fu YC (2010) Grindability and surface integrity of cast nickel-based superalloy in creep feed grinding with brazed CBN abrasive wheels. Chinese J Aeronaut 23(4):501–510
12. Wang SB, Kou HS (2006) Selections of working conditions for creep feed grinding. Part(II): workpiece temperature and critical grinding energy for burning. Int J Adv Manuf Technol 28(1–2): 38–44
13. Parente MPL, Natal Jorge RM, Aguiar Vieira A, Monteiro Baptista A (2012) Experimental and numerical study of the temperature field during creep feed grinding. Int J Adv Manuf Technol 61(1–4):127–134
14. Abdullah A, Farhadi A, Pak A (2012) Ultrasonic-assisted dry creep-feed up-grinding of superalloy Inconel738LC. Exp Mech 52(7): 843–853
15. Zhu XX, Wang WH, Jiang RS, Liu XF (2018) Study on grinding force and surface roughness of Ni_3Al based superalloy. In ASME 2018 International Mechanical Engineering Congress and Exposition (pp. V002T02A006-V002T02A006)
16. Azizi A, Mohamadyari M (2015) Modeling and analysis of grinding forces based on the single grit scratch. Int J Adv Manuf Technol 78(5–8):1223–1231
17. Li HN, Yu TB, Wang ZX, Zhu LD, Wang WS (2017) Detailed modeling of cutting forces in grinding process considering variable stages of grain-workpiece micro interactions. Int J Mech Sci 126: 319–339
18. Sunarto IY (2001) Creep feed profile grinding of Ni-based superalloys with ultrafine-polycrystalline cBN abrasive grits. Precis Eng 25(4):274–283
19. Malkin S (1989) Grinding technology: theory and applications of machining with abrasives. Wiley, Chichester
20. Ding ZS, Jiang XH, Guo MX, Liang SY (2018) Investigation of the grinding temperature and energy partition during cylindrical grinding. Int J Adv Manuf Technol 97(5–8):1767–1778
21. Guo C, Malkin S (1995) Analysis of transient temperatures in grinding. Journal of Engineering for Industry 117(4):571–577
22. Guo C, Malkin S (1996) Inverse heat transfer analysis of grinding, part 2: applications. Journal of Engineering for Industry 118(1): 143–149
23. Rowe WB (2001) Thermal analysis of high efficiency deep grinding. Int J Mach Tools Manuf 41(1):1–19
24. Lin KY, Wang WH, Jiang RS, Xiong YF, Song GD (2017) Grindability and surface integrity of in situ TiB2 particle reinforced aluminum matrix composites. Int J Adv Manuf Technol 88(1–4): 887–898
25. Di Ilio A, Paoletti A (2000) A comparison between conventional abrasives and superabrasives in grinding of SiC-aluminium composites. Int J Mach Tools Manuf 40(2):173–184